*Geophys. J. Int.* (2002) **150,** 753–769

# A new time-domain approach for the electromagnetic induction problem in a three-dimensional heterogeneous earth

Yozo Hamano

*Department of Earth and Planetary Science, University of Tokyo, Bunkyo-ku, Tokyo,* 113-0033, *Japan. E-mail: hamano@eps.s.u-tokyo.ac.jp*

Accepted 2002 March 18. Received 2002 January 1; in original form 2001 May 29

## SUMMARY

We present a new time-domain approach to the forward modelling of 3-D electromagnetic induction in a heterogeneous conducting sphere excited by external and internal sources. This method utilizes the standard decomposition of the magnetic field into toroidal and poloidal parts, and spherical harmonic expansions of both the magnetic fields and the conductivity heterogeneity. Resulting induction equations for the spherical harmonics are solved simultaneously in the time domain. Coupling terms between the electromagnetic fields and the conductivity structure are re-expanded in spherical harmonics, so that the terms can be calculated by matrix multiplications at each time step of the computation. A finite difference approximation was used to solve the set of diffusion equations for the spherical harmonics up to degree 20. This method can be efficiently used to analyse transient geomagnetic variations to estimate the 3-D conductivity structure of the Earth.

In order to validate the present approach, we solved an induction problem in simple four-layer mantle models, which consist of the surface layer ($r = 6371 - 6351$ km, $\sigma = 1$ S m$^{-1}$), the upper mantle ($r = 6351 - 5971$ km, $\sigma = 0.01$ S m$^{-1}$), the transition layer ($r = 5971 - 5671$ km, $\sigma = 0.01$–$1$ S m$^{-1}$), and the lower mantle ($r = 5671 - 3481$ km, $\sigma = 1$ S m$^{-1}$). Conductivity heterogeneities are considered in the surface layer or the transition layer. For these models, temporal variations of the Gauss coefficients in response to a sudden application of $P_1^0$-type external field were calculated, and the impulse response function of each harmonic component was obtained by differentiating the calculated variations with time. The response functions of the primary induced components, $g_1^0$, have large initial values and monotonously decay with time. Changes of the decay rate reflect the radial distribution of the electrical conductivity. For the surface heterogeneous models, temporal variations of other secondary induced components have two peaks, where the first peak (observed at 0.001–0.01 hr after the application of the external field) corresponds to the surface-layer induced phase and the second peak (1–50 hr after the onset) reflects the deeper structure. The difference of the response functions between the models with the conductivity jump at 400 km and 700 km depths becomes apparent after about 1000 s elapsed. The differences can be used to estimate the electrical conductivity structure around the transition layer. Considering that all the induced components except $g_1^0$ are generated by the surface heterogeneous layer, the surface layer should be included even for calculating the long period response functions for periods much longer than the characteristic time of the surface layer. For the model in which the transition layer is heterogeneous, the signal starts at about 1000 s after the onset and lasts more than about 100 hr. Fourier transform of the time-domain response functions gives the response function in the frequency domain, which can be compared with the previous solutions. Real and imaginary parts of the spatial distribution of the induced magnetic field in frequency domain were calculated from the present results, and compared with those calculated by the staggered-grid finite difference method. This comparison indicates that the surface induced phases are equally detected in the both approaches even for periods as long as 10 days.

**Key words:** 3-D structure, electrical conductivity, electromagnetic induction, electromagnetic modelling, numerical techniques, spherical harmonics.

## 1 INTRODUCTION

The time variations of the geomagnetic field are known to be the result of two primary processes: the secular variation of the main field of internal origin and the variation of the external field, the sources of which are located in the ionosphere and magnetosphere. Observations of these external and internal fields can be used to infer the electrical conductivity structure within the Earth. The electrical conductivity of the materials comprising the Earth's mantle is strongly dependent upon temperature, but it is also an indicator of state, composition and the presence of volatiles. Since our present knowledge of the interior of the Earth comes primarily from the elastic properties obtained by seismology, joint interpretation of seismic and EM data sets promises to constrain more strongly the geotherm, composition and state of the Earth's mantle. Global seismic tomography clearly shows the existence of lateral heterogeneities of the seismic wave velocity in the deep interiors of the mantle, and hence, the observation of the conductivity heterogeneities can give powerful clue on the dynamic state of the mantle.

The estimation of global geomagnetic response functions and their interpretation in terms of mantle electrical conductivity structure have been available for 60 years (Lahiri & Price 1939; Banks 1969; Parker 1970; Achache *et al.* 1981; Constable 1993). All these studies assume a radially symmetric conductivity structure of the Earth, and all indicate a rapid increase of the conductivity at depths between 400 and 1000 km. It became apparent with time, however, that the great variability of near-surface conductivities has a large influence on the interpretation of the deep distribution of conductivity. Furthermore, analysis of 1-D conductivity sounding profiles calculated from magnetic observatory data reveals significant regional variability in the deep mantle (Schultz 1990; Egbert & Booker 1992; Schultz *et al.* 1993; Olsen 1999). Recognizing the importance of the heterogeneous structure for the induction study, the forward modelling of electromagnetic induction in a spherical earth with a 3-D electrical conductivity structure has recently been an active field of investigation. The thin sheet concept, presented in Fainberg *et al.* (1990a,b) confines lateral variations of electrical conductivity to an inhomogeneous thin shell at the surface, which can model the effect of a large conductivity contrast between oceans and continents. The integral equation approach evolved to a method based on the modified iterative-dissipative methods to investigate the deep heterogeneous structure of the Earth (Kuvshinov *et al.* 1990, 1999). The perturbation expansion method (Zhang & Schultz 1992) models the lateral variations of mantle electrical conductivity as small perturbations about a zero-order radial profile. Schultz & Pritchard (1998) used this approach as the base for generating the first 3-D inverse model of the conductivity of the upper mantle and mid-mantle. Everett & Schultz (1996) devised a 3-D finite element forward solution using spherical polyhedra. The implementation of 3-D staggered grid finite differences to modelling 3-D global-scale electromagnetic induction was made by Uyeshima & Schultz (2000). Martinec (1999) has recently applied a spectral-finite element approach to the problem of external electromagnetic induction in an arbitrary heterogeneous conducting sphere. Tarits & Grammatica (2000) calculated the induction field at the satellite altitude due to the surface heterogeneity by using the spectral transform method described by Tarits (1994).

All the recent approaches for global earth modelling calculate the induction in frequency domain in order to investigate a steady-state part of geomagnetic variation with a strictly periodic current system flowing in the Earth. On the other hand, in electromagnetic exploration, the time domain approach is also used to estimate the crustal structure of the Earth. For the global study, the transient response is also useful to detect the conductivity structure of deep interiors of the Earth. In order to treat the transient response of the induction due to the external magnetic disturbances observed during large magnetic storms, and the sudden change of the geomagnetic field of core origin such as the magnetic jerk, I deal with the induction problem in the time domain. In addition, spherical harmonic analysis is still the most powerful method to decompose the globally observed magnetic field into the external and the internal part. Hence, the global geomagnetic field and its variations are generally expressed in terms of the Gauss coefficients of the spherical harmonic expansion of the geomagnetic potential at the surface. The purpose of the present paper is to present a time-domain approach to compute a 3-D electromagnetic response of the heterogeneous mantle to the external disturbance and the disturbances of core origin. In order to use the Gauss coefficients and their variations for the induction study, I employ the standard decomposition of the toroidal and poloidal field and the spherical harmonic expansions of the fields.

## 2 FORMULATION

We solve the following Maxwell equations for the magnetic induction **B** and the electric field **E** simultaneously, allowing that the magnetic diffusivity $\eta = 1/\sigma\mu_0$ varies as a function of position $(r, \theta, \varphi)$ in spherical coordinates:

$$\frac{\partial \mathbf{B}}{\partial t} = -\nabla \times (\eta \nabla \times \mathbf{B})$$
$$\frac{\partial \mathbf{E}}{\partial t} = -\eta \nabla \times \nabla \times \mathbf{E}, \tag{1}$$

where the relation between **E** and **B** is expressed as $\mathbf{E} = \eta \nabla \times \mathbf{B}$. Because the magnetic induction, **B**, is solenoidal (i.e. $\nabla \cdot \mathbf{B} = 0$), **B** can be decomposed into two parts: toroidal and poloidal fields as

$$\mathbf{B} = \nabla \times (T\mathbf{r}) + \nabla \times \nabla \times (P\mathbf{r}). \tag{2}$$

Substituting this relation into eq. (1), and using the relations for the angular momentum operator, $L^2$;

$$\mathbf{r} \cdot \mathbf{B} = L^2 P \quad \text{and} \quad \mathbf{r} \cdot \nabla \times \mathbf{B} = L^2 T \quad \text{where} \quad L^2 = -\left\{ \frac{1}{\sin\theta} \frac{\partial}{\partial \theta} \left( \sin\theta \frac{\partial}{\partial \theta} \right) + \frac{1}{\sin^2\theta} \frac{\partial^2}{\partial \varphi^2} \right\}, \tag{3}$$

we obtain the following two equations for the poloidal and toroidal scalar functions ($P$ and $T$) in spherical coordinates:

$$L^2\frac{\partial}{\partial t}[rP] = \eta L^2\left(\frac{\partial^2}{\partial r^2}-\frac{L^2}{r^2}\right)[rP] - \left\{\left(\frac{\partial\eta}{\partial\theta}\right)\frac{\partial}{\partial\theta}+\left(\frac{1}{\sin\theta}\frac{\partial\eta}{\partial\varphi}\right)\frac{1}{\sin\theta}\frac{\partial}{\partial\varphi}\right\}\left(\frac{\partial^2}{\partial r^2}-\frac{L^2}{r^2}\right)[rP] - \left\{\left(\frac{\partial\eta}{\partial\theta}\right)\frac{1}{\sin\theta}\frac{\partial}{\partial\varphi}-\left(\frac{1}{\sin\theta}\frac{\partial\eta}{\partial\varphi}\right)\frac{\partial}{\partial\theta}\right\}\frac{\partial}{\partial r}[rT], \tag{4}$$

$$\begin{aligned} L^2\frac{\partial}{\partial t}[rT] = {} & \eta L^2\left(\frac{\partial^2}{\partial r^2}-\frac{L^2}{r^2}\right)[rT] + \left(\frac{\partial\eta}{\partial r}\right)L^2\frac{\partial}{\partial r}[rT] + \frac{1}{r^2}(L^2\eta)L^2[rT] \\ & - \left\{\left(\frac{\partial\eta}{\partial\theta}\right)\frac{\partial}{\partial\theta}+\left(\frac{1}{\sin\theta}\frac{\partial\eta}{\partial\varphi}\right)\frac{1}{\sin\theta}\frac{\partial}{\partial\varphi}\right\}\left(\frac{\partial^2}{\partial r^2}-\frac{2L^2}{r^2}\right)[rT] \\ & - \left\{\left(\frac{\partial}{\partial\theta}\frac{\partial\eta}{\partial r}\right)\frac{\partial}{\partial\theta}+\left(\frac{1}{\sin\theta}\frac{\partial}{\partial\varphi}\frac{\partial\eta}{\partial r}\right)\frac{1}{\sin\theta}\frac{\partial}{\partial\varphi}\right\}\frac{\partial}{\partial r}[rT] \\ & + \left\{\left(\frac{\partial\eta}{\partial\theta}\right)\frac{1}{\sin\theta}\frac{\partial}{\partial\varphi}-\left(\frac{1}{\sin\theta}\frac{\partial\eta}{\partial\varphi}\right)\frac{\partial}{\partial\theta}\right\}\frac{\partial}{\partial r}\left(\frac{\partial^2}{\partial r^2}-\frac{L^2}{r^2}\right)[rP] \\ & + \left\{\left(\frac{\partial}{\partial\theta}\frac{\partial\eta}{\partial r}\right)\frac{1}{\sin\theta}\frac{\partial}{\partial\varphi}-\left(\frac{1}{\sin\theta}\frac{\partial}{\partial\varphi}\frac{\partial\eta}{\partial r}\right)\frac{\partial}{\partial\theta}\right\}\left(\frac{\partial^2}{\partial r^2}-\frac{L^2}{r^2}\right)[rP]. \end{aligned} \tag{5}$$

It can be seen from these equations that the two modes (toroidal and poloidal) are mutually coupled, and hence, the equations should be solved simultaneously. To solve the equations, we expand the scalar fields $P$ and $T$, and the magnetic diffusivity $\eta$ by the spherical harmonics as

$$\begin{aligned} \eta(r,\theta,\varphi) &= \eta^*\left[1+\sum_{n=1}^{\infty}\sum_{k=0}^{n}\left\{\eta_n^{kc}\cos k\varphi+\eta_n^{ks}\sin k\varphi\right\}P_n^k(\theta)\right] = \eta^*[1+\eta'(\theta,\varphi)] \\ P(r,\theta,\varphi) &= \sum_{l=1}^{\infty}\sum_{m=0}^{n}\left\{p_l^{mc}\cos k\varphi+p_l^{ms}\sin k\varphi\right\}P_l^m(\theta) \\ T(r,\theta,\varphi) &= \sum_{l=1}^{\infty}\sum_{m=0}^{n}\left\{t_l^{mc}\cos k\varphi+t_l^{ms}\sin k\varphi\right\}P_l^m(\theta), \end{aligned} \tag{6}$$

where the radial dependence of the conductivity is not considered in the spherical shell. Substituting these equations into eqs (4) and (5), multiplying the resulting equations by $P_n^k(\theta)^{\cos k\varphi}_{\sin k\varphi}$, and integrating over the spherical surface, we get a set of diffusion equations for each harmonic component of the poloidal and toroidal field:

$$\begin{aligned} \frac{1}{\eta^*}\frac{\partial}{\partial t}\left[rp_l^{mc\cdot s}\right]-\left(\frac{\partial^2}{\partial r^2}-\frac{l(l+1)}{r^2}\right)\left[rp_l^{mc\cdot s}\right] &= \frac{1}{l(l+1)}F_l^{mc\cdot s} \\ \frac{1}{\eta^*}\frac{\partial}{\partial t}\left[rt_l^{mc\cdot s}\right]-\left(\frac{\partial^2}{\partial r^2}-\frac{l(l+1)}{r^2}\right)\left[rt_l^{mc\cdot s}\right] &= \frac{1}{l(l+1)}G_l^{mc\cdot s}, \end{aligned} \tag{7}$$

where $p_l^{mc\cdot s}$ denotes $p_l^{mc}$ or $p_l^{ms}$, etc.

These equations are the diffusion equations with the source terms in the right hand side, and can be solved as an initial value problem, if the right-hand side of eq. (7) can be explicitly expressed with the coefficients; $\eta_n^{kc\cdot s}$, $p_l^{mc\cdot s}$, and $t_l^{mc\cdot s}$. The source terms are expressed as

$$F_l^{mc\cdot s} = \int\left[\begin{aligned} & \eta' L^2\left(\frac{\partial^2}{\partial r^2}-\frac{L^2}{r^2}\right)[rP] - \left\{\left(\frac{\partial\eta'}{\partial\theta}\right)\frac{\partial}{\partial\theta}+\left(\frac{1}{\sin\theta}\frac{\partial\eta'}{\partial\varphi}\right)\frac{1}{\sin\theta}\frac{\partial}{\partial\varphi}\right\} \\ & \times\left(\frac{\partial^2}{\partial r^2}-\frac{L^2}{r^2}\right)[rP] - \left\{\left(\frac{\partial\eta'}{\partial\theta}\right)\frac{1}{\sin\theta}\frac{\partial}{\partial\varphi}-\left(\frac{1}{\sin\theta}\frac{\partial\eta'}{\partial\varphi}\right)\frac{\partial}{\partial\theta}\right\}\frac{\partial}{\partial r}[rT]\end{aligned}\right]P_l^m(\theta)^{\cos m\varphi}_{\sin m\varphi}\,d\Omega, \tag{8}$$

$$G_l^{mc\cdot s} = \int\left[\begin{aligned} & \eta' L^2\left(\frac{\partial^2}{\partial r^2}-\frac{L^2}{r^2}\right)[rT] + \frac{1}{r^2}\left(L^2\eta'\right)L^2[rT] \\ & - \left\{\left(\frac{\partial\eta'}{\partial\theta}\right)\frac{\partial}{\partial\theta}+\left(\frac{1}{\sin\theta}\frac{\partial\eta'}{\partial\varphi}\right)\frac{1}{\sin\theta}\frac{\partial}{\partial\varphi}\right\}\left(\frac{\partial^2}{\partial r^2}-\frac{2L^2}{r^2}\right)[rT] \\ & + \left\{\left(\frac{\partial\eta'}{\partial\theta}\right)\frac{1}{\sin\theta}\frac{\partial}{\partial\varphi}-\left(\frac{1}{\sin\theta}\frac{\partial\eta'}{\partial\varphi}\right)\frac{\partial}{\partial\theta}\right\}\frac{\partial}{\partial r}\left(\frac{\partial^2}{\partial r^2}-\frac{L^2}{r^2}\right)[rP]\end{aligned}\right]P_l^m(\theta)^{\cos m\varphi}_{\sin m\varphi}\,d\Omega. \tag{9}$$

For a complex spherical surface harmonics $Y_l^m(\theta,\varphi)=P_l^m(\theta)e^{im\varphi}(-l\le m\le l)$, the integral,

$$A^{m_1,m_2,m_3}_{l_1,l_2,l_3} = \int Y_{l_1}^{m_1}Y_{l_2}^{m_2}Y_{l_3}^{m_3}\,d\Omega, \tag{10}$$

has been known as Adams integral in the geomagnetic community or Gaunt integral in atomic physics (James 1973). The Elsasser integral

$$E^{m_1,m_2,m_3}_{l_1,l_2,l_3} = \int \left( \frac{\partial Y^{m_1}_{l_1}}{\partial\theta}\frac{\partial Y^{m_2}_{l_2}}{\sin\theta\partial\varphi} - \frac{\partial Y^{m_1}_{l_1}}{\sin\theta\partial\varphi}\frac{\partial Y^{m_2}_{l_2}}{\partial\theta} \right) Y^{m_3}_{l_3}\, d\Omega, \tag{11}$$

is also used in the geomagnetic dynamo theory, which can be reduced to a linear combination of the Adams-Gaunt integrals. The Adams-Gaunt integral was evaluated and tabulated as Wigner (or Clebsch–Gordan) coefficients and widely used in quantum mechanics. Although the present integrals in eqs (8) and (9) are also expressed by the Wigner/Clebsch–Gordan coefficients and obtain the values from the extensive tables of the coefficients, we try to derive the explicit expression of the integrals with the coefficients of the spherical harmonic expansions in order to solve the equations by numerical computation. For that purpose, we need to expand the integrands in eqs (8) and (9) with the linear combination of spherical harmonics.

By substituting the coupling terms in the integrands, i.e., $\eta' P$, $(\frac{\partial\eta'}{\partial\theta})(\frac{\partial P}{\partial\theta})$, $(\frac{1}{\sin\theta}\frac{\partial\eta'}{\partial\varphi})(\frac{1}{\sin\theta}\frac{\partial P}{\partial\varphi})$, $(\frac{\partial\eta'}{\partial\theta})(\frac{1}{\sin\theta}\frac{\partial P}{\partial\varphi})$, $(\frac{1}{\sin\theta}\frac{\partial\eta'}{\partial\varphi}\frac{\partial P}{\partial\theta})$ and similar expressions for $T$, with the expressions in eq. (6), the coupling terms can be expressed with the linear combinations of

$$\eta^{kc\cdot s}_n p^{mc\cdot s}_l P^k_n P^m_l \begin{matrix}\cos(m+k)\varphi \\ \sin(m+k)\varphi\end{matrix}, \quad \eta^{kc\cdot s}_n p^{mc\cdot s}_l P^k_n P^m_l \begin{matrix}\cos(|m-k|)\varphi \\ \sin(|m-k|)\varphi\end{matrix},$$

$$\eta^{kc\cdot s}_n p^{mc\cdot s}_l \frac{dP^k_n}{d\theta}\frac{dP^m_l}{d\theta} \begin{matrix}\cos(m+k)\varphi \\ \sin(m+k)\varphi\end{matrix}, \quad \eta^{kc\cdot s}_n p^{mc\cdot s}_l \frac{dP^k_n}{d\theta}\frac{dP^m_l}{d\theta} \begin{matrix}\cos(|m-k|)\varphi \\ \sin(|m-k|)\varphi\end{matrix},$$

$$\eta^{kc\cdot s}_n p^{mc\cdot s}_l \frac{k}{\sin\theta}P^k_n \frac{m}{\sin\theta}P^m_l \begin{matrix}\cos(m+k)\varphi \\ \sin(m+k)\varphi\end{matrix}, \quad \eta^{kc\cdot s}_n p^{mc\cdot s}_l \frac{k}{\sin\theta}P^k_n \frac{m}{\sin\theta}P^m_l \begin{matrix}\cos(|m-k|)\varphi \\ \sin(|m-k|)\varphi\end{matrix},$$

$$\eta^{kc,s}_n p^{mc,s}_l \frac{dP^k_n}{d\theta}\frac{m}{\sin\theta}P^m_l \begin{matrix}\cos(m+k)\varphi \\ \sin(m+k)\varphi\end{matrix}, \quad \eta^{kc,s}_n p^{mc,s}_l \frac{dP^k_n}{d\theta}\frac{m}{\sin\theta}P^m_l \begin{matrix}\cos(|m-k|)\varphi \\ \sin(|m-k|)\varphi\end{matrix},$$

$$\eta^{kc,s}_n p^{mc,s}_l \frac{k}{\sin\theta}P^k_n \frac{dP^m_l}{d\theta} \begin{matrix}\cos(m+k)\varphi \\ \sin(m+k)\varphi\end{matrix}, \quad \eta^{kc,s}_n p^{mc,s}_l \frac{k}{\sin\theta}P^k_n \frac{dP^m_l}{d\theta} \begin{matrix}\cos(|m-k|)\varphi \\ \sin(|m-k|)\varphi\end{matrix},$$

respectively. Since the derivatives of the spherical harmonics with respect to $\theta$ and $\varphi$ are expressed with the sum of the single spherical harmonics by using the recursive relations of the Legendre functions (see e.g. Abramowitz & Stegun 1965), the coupling terms can all be expressed with the linear combinations of

$$P^k_n P^m_l \begin{matrix}\cos(m+k)\varphi \\ \sin(m+k)\varphi\end{matrix} \quad \text{and} \quad P^k_n P^m_l \begin{matrix}\cos(|m-k|)\varphi \\ \sin(|m-k|)\varphi\end{matrix}.$$

The above two terms can be decomposed into the linear combinations of the single spherical harmonics by using the relations of

$$P^k_n P^m_l = \sum_{s=0}^{s_{n+}} \left(Q^{n,k}_{l,m}\right)_s P^{k+m}_{n+l-2s}, \qquad s_{n+} = \left[\frac{n+l-(k+m)}{2}\right] \tag{12}$$

and

$$P^k_n P^m_l = \sum_{s=0}^{s_{n-}} \left(R^{n,k}_{l,m}\right)_s P^{|k-m|}_{n+l-2s}, \qquad s_{n-} = \left[\frac{n+l-|k-m|}{2}\right], \tag{13}$$

respectively, where the coefficients $(Q^{n,k}_{l,m})_s$ and $(R^{n,k}_{l,m})_s$ are shown in Appendix A and B. Hence, the coupling terms in the integrands are all expressed with the sum of the sets of spherical harmonics, and the integration of these terms in eqs (8) and (9) can be expressed with the expansion coefficients defined in eq. (6).

Finally, $F^{mc\cdot s}_l$ and $G^{mc\cdot s}_l$ in eqs (8) and (9) are simplified as

$$F^{mc\cdot s}_l = \sum_{n,kc\cdot s} (\Psi_0)^{l,mc\cdot s}_{n,kc\cdot s} n(n+1)\left(\frac{\partial^2}{\partial r^2} - \frac{n(n+1)}{r^2}\right)\left[r p^{kc\cdot s}_n\right] - \sum_{n,kc\cdot s} (\Psi_+)^{l,mc\cdot s}_{n,kc\cdot s}\left(\frac{\partial^2}{\partial r^2} - \frac{n(n+1)}{r^2}\right)\left[r p^{kc\cdot s}_n\right] - \sum_{n,kc\cdot s} (\Psi_-)^{l,mc\cdot s}_{n,kc\cdot s}\frac{\partial}{\partial r}\left[r t^{kc\cdot s}_n\right] \tag{14}$$

and

$$\begin{aligned} G^{mc\cdot s}_l = &\sum_{n,kc\cdot s} (\Psi_0)^{l,kc\cdot s}_{n,kc\cdot s} n(n+1)\left(\frac{\partial^2}{\partial r^2} - \frac{n(n+1)}{r^2}\right)\left[r t^{kc\cdot s}_n\right] - \sum_{n,kc\cdot s} (\Psi_+)^{l,kc\cdot s}_{n,kc\cdot s}\left(\frac{\partial^2}{\partial r^2} - \frac{2n(n+1)}{r^2}\right)\left[r t^{kc\cdot s}_n\right] \\ &- \sum_{n,kc\cdot s} l(l+1)(\Psi_0)^{l,kc\cdot s}_{n,kc\cdot s}\frac{n(n+1)}{r^2}\left[r t^{kc\cdot s}_n\right] - \sum_{n,kc\cdot s} (\Psi_-)^{l,kc\cdot s}_{n,kc\cdot s}\frac{\partial}{\partial r}\left(\frac{\partial^2}{\partial r^2} - \frac{n(n+1)}{r^2}\right)\left[r p^{kc\cdot s}_n\right] \end{aligned} \tag{15}$$

by using the three operators, $\Psi_o$, $\Psi_+$, $\Psi_-$, defined as

$$[\eta' P]_l^{mc\cdot s} = \Psi_o P = \sum_{n,kc\cdot s} (\Psi_o)_{n,kc\cdot s}^{l,mc\cdot s} p_n^{kc\cdot s},$$

$$\left[\left\{\left(\frac{\partial \eta'}{\partial \theta}\right)\frac{\partial}{\partial \theta} + \left(\frac{1}{\sin\theta}\frac{\partial \eta'}{\partial \varphi}\right)\frac{1}{\sin\theta}\frac{\partial}{\partial \varphi}\right\} P\right]_l^{mc,s} = \Psi_+ P = \sum_{n,kc\cdot s} (\Psi_+)_{n,kc\cdot s}^{l,mc\cdot s} p_n^{kc\cdot s}, \tag{16}$$

$$\left[\left\{\left(\frac{\partial \eta'}{\partial \theta}\right)\frac{1}{\sin\theta}\frac{\partial}{\partial \varphi} - \left(\frac{1}{\sin\theta}\frac{\partial \eta'}{\partial \varphi}\right)\frac{\partial}{\partial \theta}\right\} P\right]_l^{mc,s} = \Psi_- P = \sum_{n,kc\cdot s} (\Psi_-)_{n,kc\cdot s}^{l,mc\cdot s} p_n^{kc\cdot s},$$

where $[\cdot]_l^{mc,s}$ denotes the integral $\int \cdot P_l^m(\theta)_{\sin m\varphi}^{\cos m\varphi}\, d\Omega$. Since the three operators are only functions of the structure, i.e. the function of the lateral heterogeneity of the magnetic diffusivity, and do not depend on the magnetic field, the operators can be calculated before the time integration of the field using eq. (7).

## 3 NUMERICAL CALCULATION

### 3.1 A simple earth model with a surface heterogeneous layer

In order to verify the present time-domain approach to the induction in a 3-D Earth, we calculate the induction of simple 4-layer mantle models of the Earth. The models are shown in Fig. 1. The four layers consist of the surface layer ($r = 6371 - 6351$ km), the upper mantle ($r = 6351 - 5971$ km), the transition layer ($r = 5971 - 5671$ km), and the lower mantle ($r = 5671 - 3481$ km). Model H is a homogeneous mantle model with $\sigma = 1$ S m$^{-1}$. In model400 and model700, the surface thin layer with a thickness of 20 km is considered as a simplification of the surface distribution of oceans and continents. The electrical resistivity in this layer is laterally heterogeneous and the distribution of the magnetic diffusivity is given by

$$\eta(\theta, \varphi) = \eta^* \left(1 + w P_1^1(\theta) \cos\varphi\right), \tag{17}$$

where $\eta^* = 1/\sigma (= 1$ S m$^{-1})$ $\mu_0$ and $w = 0.9$. The underlying layer is laterally homogeneous with a conductivity of 0.01 S m$^{-1}$. It is now generally agreed that the electrical conductivity rises from about 0.01–1 S m$^{-1}$ between the upper mantle and a depth between 400–1000 km (Petersons & Constable 1996). Hence, two models with the depth of the bottom of the second layer of 400 km (Model400) and 700 km

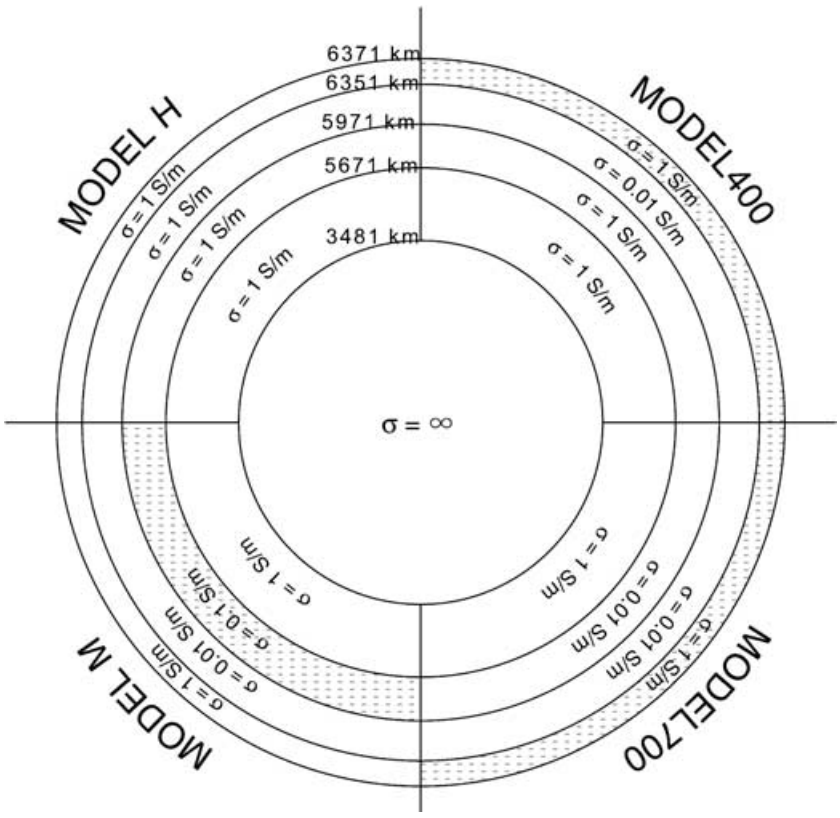


**Figure 1.** A sketch of the four-layer mantle models. The hatched layer indicates the conductivity heterogeneity. Model H: homogeneous mantle model, Model400 and Model700: The surface layer has the electrical conductivity heterogeneity given by eq. (17), and the underlying resistive layer extend to $r = 5971$ km and 5671 km, respectively. Model M: The transition layer ($r = 5971 - 5671$ km) has the conductivity heterogeneity.

(Model700) are considered in the present study. The conductivity of the lower mantle is assumed to be 1 S m$^{-1}$. In Model M, the conductivity heterogeneity ($\sigma = 0.1$ S m$^{-1}$ and $w = 0.9$) is assumed in the transition layer.

For these models, we calculated the temporal variation of the electromagnetic fields in response to a sudden application of the external field of

$$q_1^0(\theta, \varphi) = P_1^0(\theta), \tag{18}$$

at $t = 0$. Time derivative of the field induced by this abrupt change of the external field gives the impulse response function of the induced field in time domain.

### 3.2 Numerical method

For the numerical calculation, we approximate the time and the space derivatives with finite differences. Then, if we denote

$$u_j^n = rp_l^{mc\cdot s}(t_n, r_j) \quad \text{or} \quad rt_l^{mc\cdot s}(t_n, r_j), \tag{19}$$

and

$$h_j^n = F_l^{mc\cdot s}(t_n, r_j) \quad \text{or} \quad G_l^{mc\cdot s}(t_n, r_j), \tag{20}$$

finite difference approximation of eq. (7) becomes

$$\begin{aligned} &-D\frac{\Delta t}{2\Delta x^2}u_{j-1}^{n+1} + \left(1 + D\frac{\Delta t}{\Delta x^2} + D\frac{l(l+1)\Delta t}{2(1+(j-1)\Delta x)^2}\right)u_j^{n+1} - D\frac{\Delta t}{2\Delta x^2}u_{j+1}^{n+1} \\ &= D\frac{\Delta t}{2\Delta x^2}u_{j-1}^{n} + \left(1 - D\frac{\Delta t}{\Delta x^2} - D\frac{l(l+1)\Delta t}{2(1+(j-1)\Delta x)^2}\right)u_j^{n} + D\frac{\Delta t}{2\Delta x^2}u_{j+1}^{n} + D\frac{\Delta t}{l(l+1)}h_j^n, \end{aligned} \tag{21}$$

where we use the Crank–Nicholson scheme (see e.g. Press *et al.* 1992), which uses the average of the forward and backward schemes for representing the time derivative, to approximate the diffusion term of the equation for the stability of the computation, and $\Delta t$, $\Delta x$, and $D$ denote the time step, the grid spacing and the magnetic diffusivity in non-dimensional form, respectively. We used the radius of the Earth, $a = 6371$ km as the unit of length, and the diffusion time, $\tau = \sigma\mu_0 a^2 (\sigma = 1$ S m$^{-1})$, as the unit of time. In the present model, mesh divisions are 6, 9, 7, and 19 for the top, the second, the third and the bottom layers respectively, and the grid points are numbered as $j_s = 1$ for the surface, $j_{b1} = 7$ for the first boundary, $j_{b2} = 16$ for the second boundary, $J_{b3} = 22$, and $j_{b\mathrm{tm}} = 41$ for the bottom boundary. For this mesh division and the truncation level of harmonic degree 20, it took about an hour for 102 400 steps of the calculation with 667 MHz Alpha 21 264 CPU.

Boundary conditions are expressed as

$$\left\langle p_l^{mc\cdot s}\right\rangle = \left\langle t_l^{mc\cdot s}\right\rangle = \left\langle \frac{dp_l^{mc\cdot s}}{dr}\right\rangle = \left\langle \left[\eta\frac{dT}{dr}\right]_l^{mc\cdot s}\right\rangle = 0, \tag{22}$$

where $\langle\cdots\rangle$ denotes the jump across the boundary. For $u = rp_l^{mc\cdot s}$, finite difference approximation of the boundary condition at the internal boundary $j = j_b$ is given by

$$-\frac{\Delta x_+}{\Delta x_- + \Delta x_+}u_{jb-1}^{n+1} + u_{jb}^{n+1} - \frac{\Delta x_-}{\Delta x_- + \Delta x_+}u_{jb+1}^{n+1} = 0, \tag{23}$$

where $\Delta x_-$ and $\Delta x_+$ denote the grid spacing of the upper and the lower layers, respectively. For $u = rt_l^{mc\cdot s}$, the boundary condition can be expressed as

$$-\frac{D_-\Delta x_+}{D_+\Delta x_- + D_-\Delta x_+}u_{jb-1}^{n+1} + u_{jb}^{n+1} - \frac{D_+\Delta x_-}{D_+\Delta x_- + D_-\Delta x_+}u_{jb+1}^{n+1} = 0, \tag{24}$$

if the upper and the lower layers are homogeneous, whereas, if the upper boundary is heterogeneous, the condition becomes as

$$-\frac{D_-\Delta x_+}{D_+\Delta x_- + D_-\Delta x_+}u_{jb-1}^{n+1} + u_{jb}^{n+1} - \frac{D_+\Delta x_-}{D_+\Delta x_- + D_-\Delta x_+}u_{jb+1}^{n+1} = -\frac{D_-\Delta x_+}{D_+\Delta x_- + D_-\Delta x_+}\eta'\left(u_{jb}^n - u_{jb-1}^n\right), \tag{25}$$

where $D_-$ and $D_+$ denote the magnetic diffusivity of the upper and the lower layers, respectively. A similar expression can be obtained if the lower layer is heterogeneous.

The surface ($j = 1$) boundary conditions for the poloidal fields are given by

$$\left(l + \frac{r}{\Delta x_1}\right)u_1^{n+1} - \frac{r}{\Delta x_1}u_2^{n+1} = -\frac{2l+1}{l+1}v_1^{n+1}, \tag{26}$$

where $v = rq_l^m$ denotes the coefficients of the external field at the surface. For the toroidal fields, all the components are set to zero at the surface boundary. At the bottom boundary, all the poloidal and toroidal components are set to zero assuming that the conductivity of the core is much higher than the overlying mantle.

In the present study, time variations of the spherical harmonics up to degree 20 were calculated. The time variation of the internal component of the field was calculated with a time step of about 5 s and until about 730 hr. Above the Earth's surface, the magnetic induction **B** can be expressed by a gradient of the magnetic potential $V$ as $\mathbf{B} = -\nabla V$, where $V$ is expanded into spherical harmonics as

$$V = a \sum_{l=1}^{\infty} \sum_{m=0}^{l} \left\{ \left[ g_l^m \cos m\varphi + h_l^m \sin m\varphi \right] \left( \frac{a}{r} \right)^{l+1} + \left[ q_l^m \cos m\varphi + s_l^m \sin m\varphi \right] \left( \frac{r}{a} \right)^{l} \right\} P_l^m(\theta), \tag{27}$$

where $(g_l^m, h_l^m)$ and $(q_l^m, s_l^m)$ are the internal and the external Gauss coefficients, respectively.

From the surface boundary condition, the magnetic potential $V$ is related to the poloidal scalar function $P$ as $V = -\frac{\partial}{\partial r}(rP)$. Hence, the internal Gauss coefficients can be calculated from the applied external field and the surface variation of $p_l^{mc\cdot s}$ as

$$\begin{aligned} g_l^m &= l\left(p_l^{mc}\right)_1 + \frac{l}{l+1}\left(q_l^{mc}\right), \\ h_l^m &= l\left(p_l^{ms}\right)_1 + \frac{l}{l+1}\left(q_l^{ms}\right), \end{aligned} \tag{28}$$

at the surface. The calculated response of the induced field was differentiated with time to obtain the impulse response of the present earth model.

### 3.3 Induction of a homogeneous sphere

In order to check the effectiveness of the finite difference approximation, we first calculated the impulse response of a homogeneous sphere (Model H) and compared with the analytical solution (Chapman & Bartels 1940). In this model, 1 S m$^{-1}$ is assigned for the mantle conductivity. The calculated impulse response (C) is compared with the analytical solutions (T) in Fig. 2. Except the initial few steps, the calculated impulse response well reproduces the analytical response. The difference is more closely shown in Fig. 2(b), where the relative per cent-deviation of the response, (T-C)/C*100, is shown as a function of log $t$. After 0.3 hr from the onset, the fit is extremely well with the root mean square deviation of less than 0.1 per cent. The large deviation before 0.03 hr reflects the insufficiency of the finite difference approximation of the differentiation in time because of the rapid variation of the response. The deviation of about 1 per cent observed at around 0.1 hr is caused by the finite difference approximation of the boundary condition, eq. (15), because the radial gradient of the response function is large in the initial stage around the surface layer. The deviation can be reduced by decreasing the grid spacing. In summary, the present code of the finite difference equation well approximates the analytical solution for the time span longer than 0.03 hr.

### 3.4 Models with surface heterogeneities (Model400 and Model700)

Next, we calculated the impulse response functions of the two surface heterogeneous models (Model400 and Model700). In order to evaluate the effect of the truncation of the harmonic degree, temporal variations of the mean square field strength were calculated by changing the truncation level. For the Schmidt normalization, the mean square field strength of the magnetic field for the harmonic degree l is given by

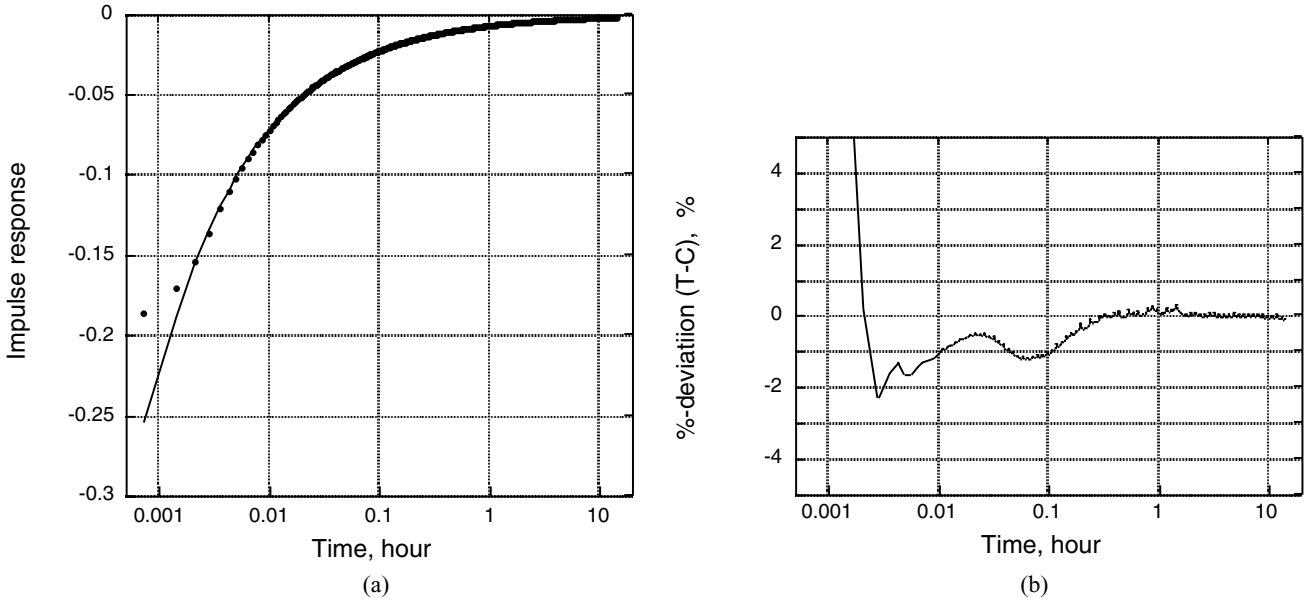


**Figure 2.** (a) Impulse response function of a homogeneous sphere corresponding to the $P_1^0$-type external source. Solid curve shows the analytical solution, whereas the black dots indicate the results of the present calculation for MODEL H. (b) per cent-deviation between the analytical solution and the present result.

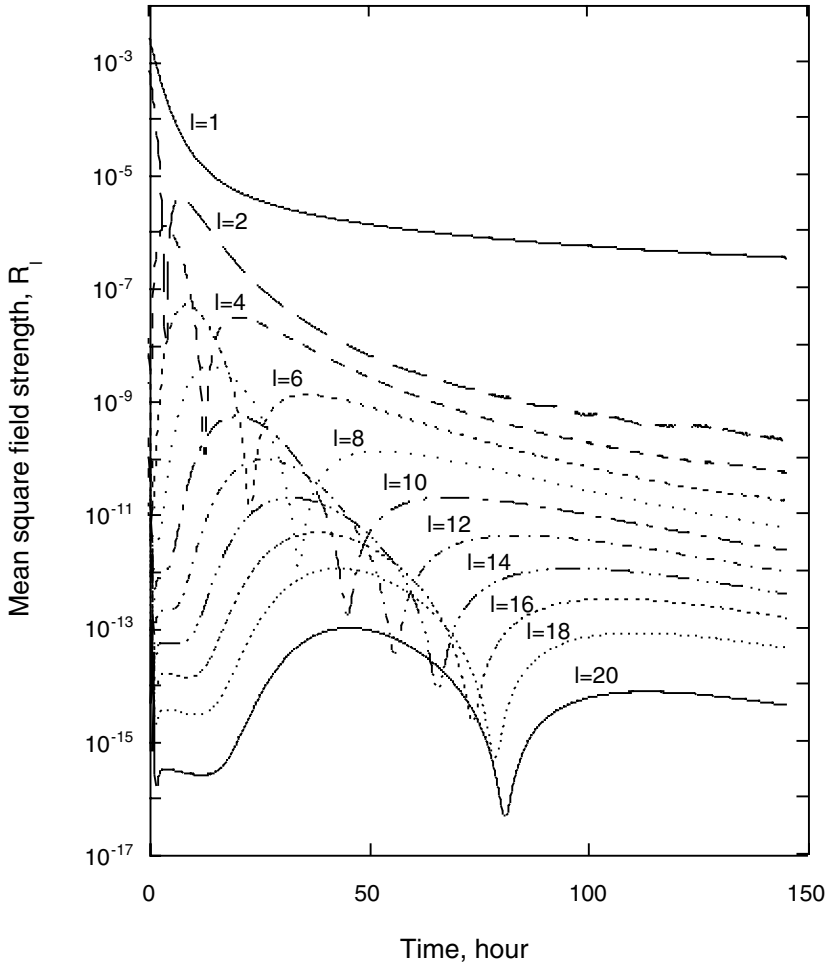


**Figure 3.** Time variations of the mean square field strength at surface corresponding to the harmonic terms of degrees $l = 1$, 2, 4, 6, 8, 10, 12,14, 16, 18 and 20.

$$R_l = (l+1)\sum_{m=0}^{l}\left(\left[g_l^m\right]^2 + \left[h_l^m\right]^2\right). \tag{29}$$

The time variations of $R_l$ are shown in Fig. 3 for the harmonic degrees of 1, 2, 4, . . . , 20. As shown in the figure, the power of the induced field rapidly decreases with the increase of the harmonic degree. Besides the initial induction, the time variations take a peak, the time of which delays with the increase of the harmonic degree. The peak values are plotted as a function of the harmonic degree in Fig. 4, where the results of the calculations with the truncation levels of 8, 12, 16 and 20 are shown. As evident from Fig. 4, the total power of the response functions can be approximated to about an accuracy of $10^{-6}$ if the coefficients up to degree 10 are used to calculate the total response functions. If the truncation level of the harmonic degree is $n$, only the coefficients of degree $n$ and $n - 1$ are severely affected by the truncation. Considering these facts, we used the coefficients up to degree 10 to calculate the spatial distribution of the response functions, although the time integral of the induction equations was made for the harmonics up to degree 20.

Now we return to the individual components of the response functions. The response functions for the dominant phases are shown in Fig. 5 as a function of log $t$, where the responses for the two models (Model400 and Model700) are compared. In Fig. 5, the amplitude of the response functions is normalized to that of the applied external field. Among the induced fields, $g_1^0$ and $g_2^1$ components are the primary induced phases. Initial inductions of these components are large and exponentially decay with time. The changes of the decay rate in this diagram correspond to the radial conductivity structure of the model. The difference of the two models (Model400 and Model700) can be observed after 0.3 hr, suggesting the possibility to estimate the depth of the conductivity jump at around this timescale. Compared to these primary induced phases, time variations of the secondary induced phases are quite different. Dominant components of these secondary phases are odd-degree zonal fields of $g_3^0$, $g_5^0$, $g_7^0$ . . . , and $g_3^2$, $g_4^1$, $g_4^3$, $g_5^2$, $g_6^1$, $g_6^3$, $g_6^5$, $g_7^2$, $g_7^4$ . . . , etc. These components are generated by the interactions between the primary and the secondary induced phases, and the heterogeneous conductivity structure in the first layer. These secondary phases have double peaks at around 0.005–0.1 hr and around 1–20 hr (for harmonic degrees 2–7) after the onset. The induced current for the first peak can be attributed to the current flow within the surface heterogeneous layer and the top of the upper mantle, because the response functions for Model400 and Model700 are identical. The splitting of the first peak corresponds to the double-peak distribution of the conductivity in the surface layer.

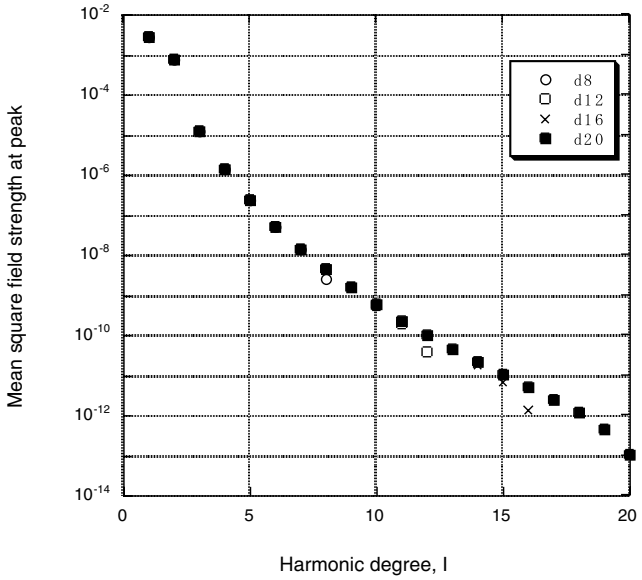


**Figure 4.** Power spectrum of the mean square field strength at peak as a function of harmonic degree *l*. Results of the calculation for the truncation degrees of 8, 12, 16 and 20 are shown.

On the other hand, the current system generating the second peak flows into the lower mantle and returns to the surface. This timescale might be important to determine the depth of the conductivity jump from the secondary induced phases, as well as the slope change of the primary induced phases. It is to be noted that the second peak in these secondary phases delays as a function of the harmonic degree. Since the harmonic degree corresponds to the wavenumber of the field, this suggests that the short wavelength signals become relatively dominant at the later stages of the responses. As will be shown later, these small scale disturbances are confined in the small region around the point (180E, 0N), where the conductivity takes a maximum value.

### 3.5 Mid-mantle heterogeneous model (Model M)

Response functions are calculated for Model M, in which the transition layer has a conductivity heterogeneity. The response functions of $g_1^0$ is very similar to the previous model shown in Fig. 5(a). Impulse responses of other harmonic components are shown in Fig. 6. The dominant induced components in Model M are the same as in the previous models, although their temporal variations are different. The impulse responses of these phases appear after 0.3 hr has elapsed from the onset. This delay corresponds to the depth of the top of the heterogeneous layer. They take a peak value around the time between 3–10 hr. Except $g_2^1$, the temporal position of the peaks roughly coincides with the second peaks observed in the respective components of Model400.

### 3.6 Space–time variation of the response function

From the Gauss coefficients, three components of the magnetic induction can be calculated as

$$
\begin{aligned}
B_z &= -B_r = \frac{\partial V}{\partial r} = -\sum_{l=1}^{\infty}\sum_{m=0}^{l}\left(\frac{a}{r}\right)^{l+2}(l+1)\left\{g_l^m\cos m\varphi + h_l^m \sin m\varphi\right\}P_l^m(\theta),\\
B_x &= -B_\theta = \frac{\partial V}{r\partial\theta} = \sum_{l=1}^{\infty}\sum_{m=0}^{l}\left(\frac{a}{r}\right)^{l+2}\left\{g_l^m\cos m\varphi + h_l^m \sin m\varphi\right\}\frac{dP_l^m(\theta)}{d\theta},\\
B_y &= B_\varphi = -\frac{\partial V}{r\sin\theta\partial\varphi} = \sum_{l=1}^{\infty}\sum_{m=0}^{l}\left(\frac{a}{r}\right)^{l+2} m\left\{g_l^m\sin m\varphi - h_l^m\cos m\varphi\right\}P_l^m(\theta),
\end{aligned}
\tag{30}
$$

where $x$ (northward), $y$ (eastward), and $z$ (downward) denote a local coordinate. Behaviour of the response function of the present simple earth can be more clearly understood when we observe the spatial distribution of the induced field. In Fig. 7, maps of the vertical component, $B_z$, of the induced field on the surface are shown, where the conductive ocean hemisphere spans from the latitude 90–270 E. In the figure, the field due to $g_1^0$ component is removed so that we can clearly observe the secondary induced phases. Therefore, the initially induced field is dominated by the $g_2^1$ component, and the amplitude is symmetric between the two hemispheres. These fields rapidly decrease with time, but the decay rate is more gradual in the ocean hemisphere. Hence, after an hour, the induced field in the ocean hemisphere becomes larger than that of the continental hemisphere. This tendency increases with time, and after 4 hr, the return current from the lower mantle causes new anomalies at the high latitudes in the ocean hemisphere. These anomalies have opposite polarity with the initially induced field, and they

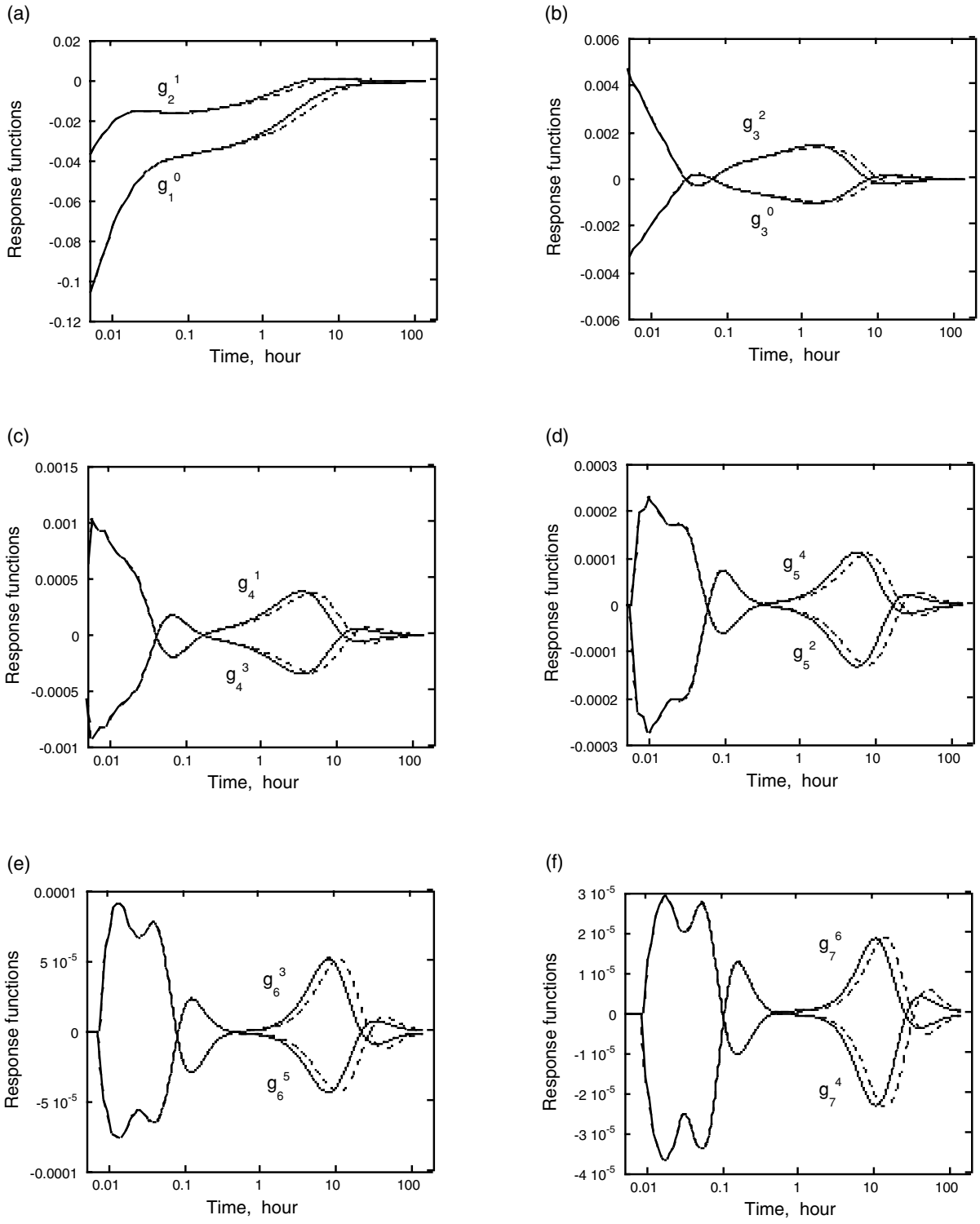


**Figure 5.** Variations of the response functions of the dominant harmonic components for Model400 (solid line) and Model700 (dashed line) as a function of log $t$. (a) $g_1^0$ and $g_2^1$, (b) $g_3^0$ and $g_3^2$, (c) $g_4^1$ and $g_4^3$, (d) $g_5^2$ and $g_5^4$, (e) $g_6^3$ and $g_6^5$, and (f) $g_7^4$ and $g_7^6$.

grow with time and move to the lower latitude. After 12 hr, these anomalies with the opposite polarity occupy the ocean hemisphere and the initially induced phase is confined within the small area around (180E, 0N), where the conductivity is maximum. After that, the size and the amplitude of the anomaly decrease with time, but it remains even after 3 days as shown in Fig. 7, and can be detected even after 30 days, although the amplitude of the anomaly is about an order of magnitude smaller than that after 3 days.

Since all the presently observed induced fields are originally induced in the surface heterogeneous layer with a thickness of only 20 km, it is to be noted that this surface heterogeneous layer should be included in the model even if the purpose of the investigation is the middle

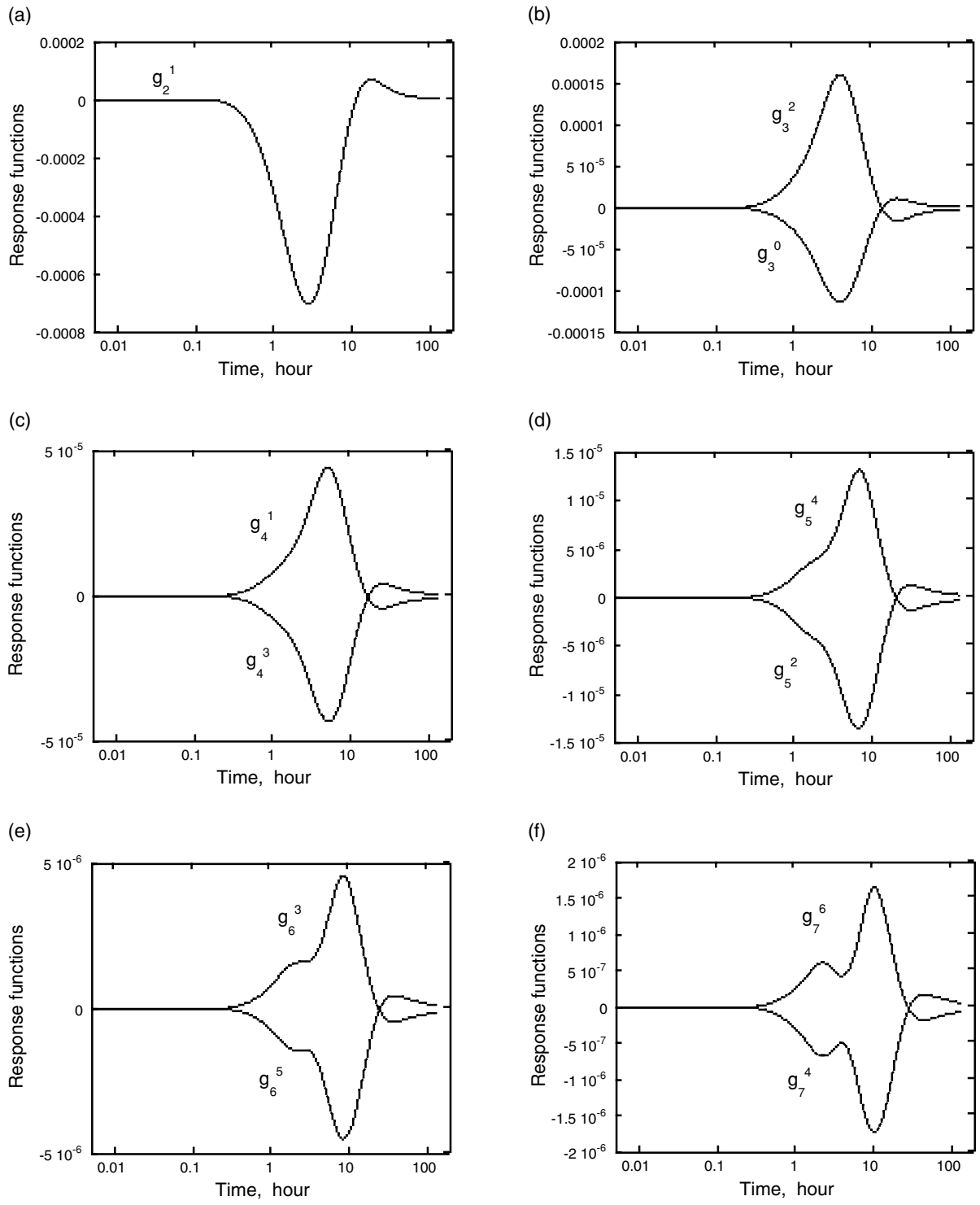


**Figure 6.** Variations of the response functions of the dominant harmonic components for Model M as a function of log $t$. (a) $g_2^1$, (b) $g_3^0$ and $g_3^2$, (c) $g_4^1$ and $g_4^3$, (d) $g_5^2$ and $g_5^4$, (e) $g_6^3$ and $g_6^5$, and (f) $g_7^4$ and $g_7^6$.

and the lower mantle. In addition, the difference of the response functions of the present two models (Model400 and Model700) suggests that the surface induced field at a timescale of 1–100 hr is important to estimate the conductivity structure of the middle mantle.

### 3.7 Response functions in frequency domain

Fourier transforms of the time-domain responses of the Gauss coefficients give the response function in the frequency domain, which can be used to compare the present results with the previous solutions. From the impulse response functions obtained in time domain (TDM solution),

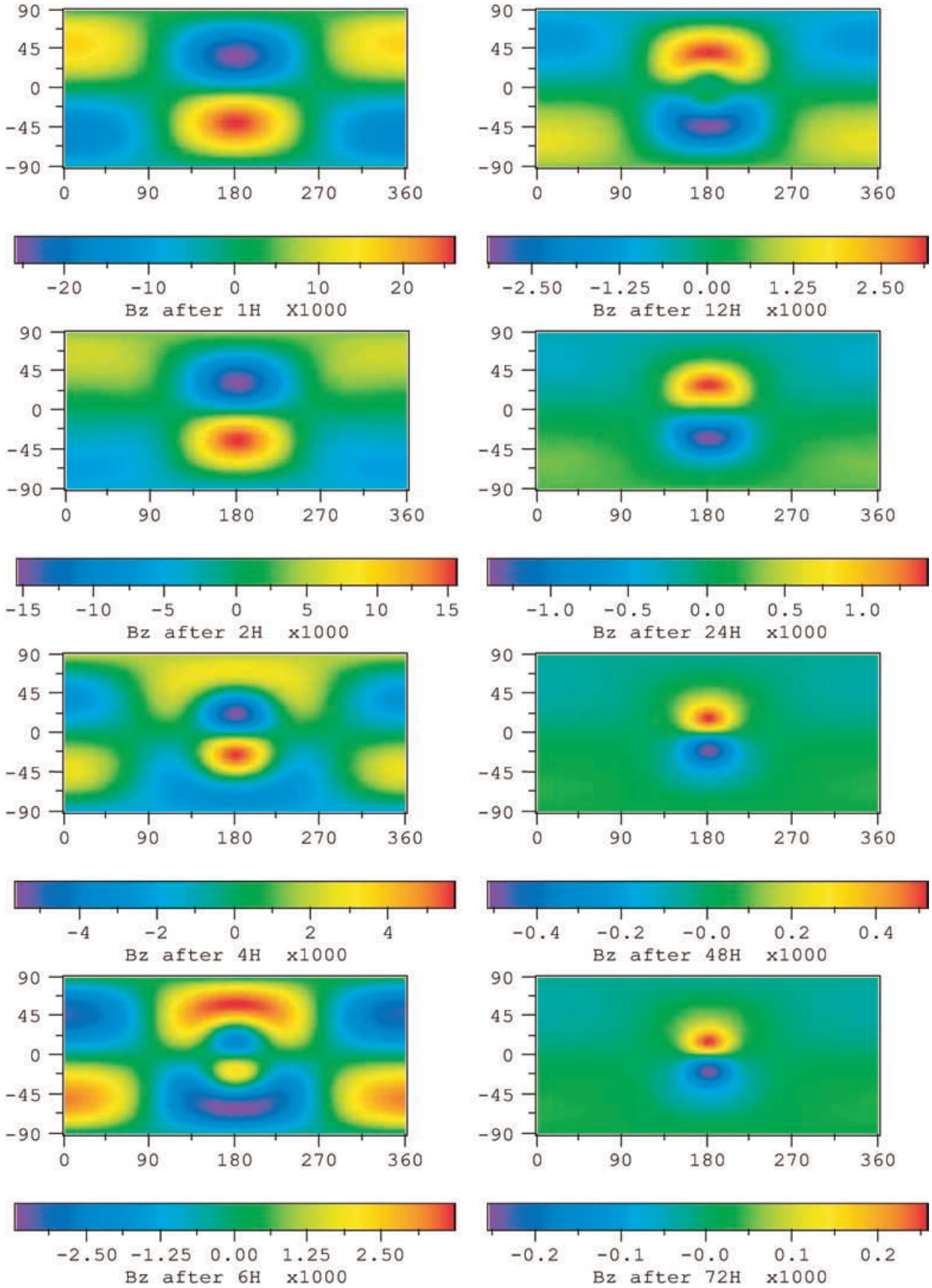


**Figure 7.** Temporal variations of the spatial distribution of $B_z$ on the Earth's surface. Scales are in the unit of the inducing external field and multiplied by 1000.

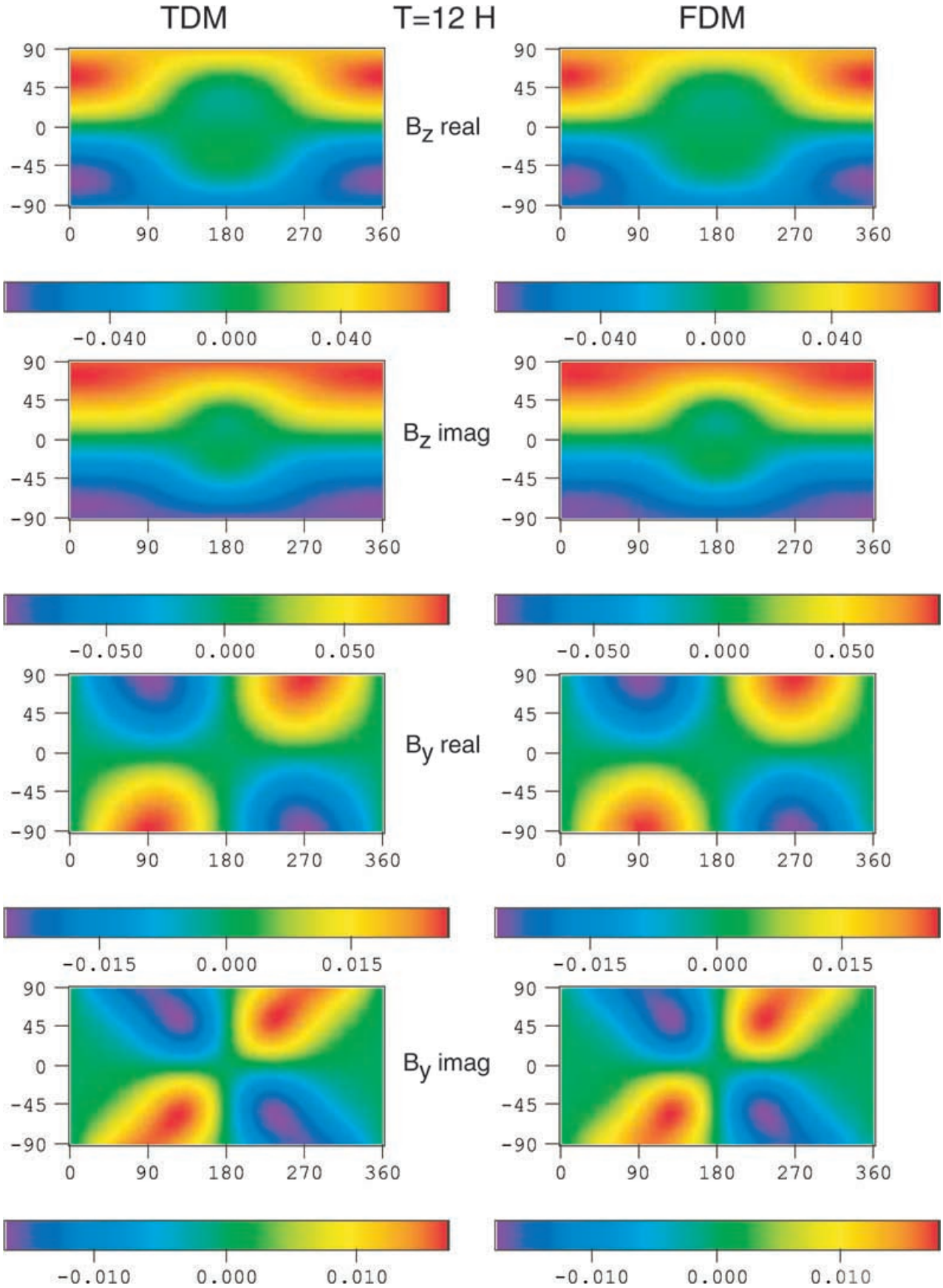


**Figure 8.** Comparison of the response functions in frequency domain between the present time domain solution (TDM) and the staggered grid finite difference solution (FDM). Real and imaginary parts of $B_z$ and $B_y$ at a period of 12 hr are shown. Scales are normalized to the amplitude of the external source field.

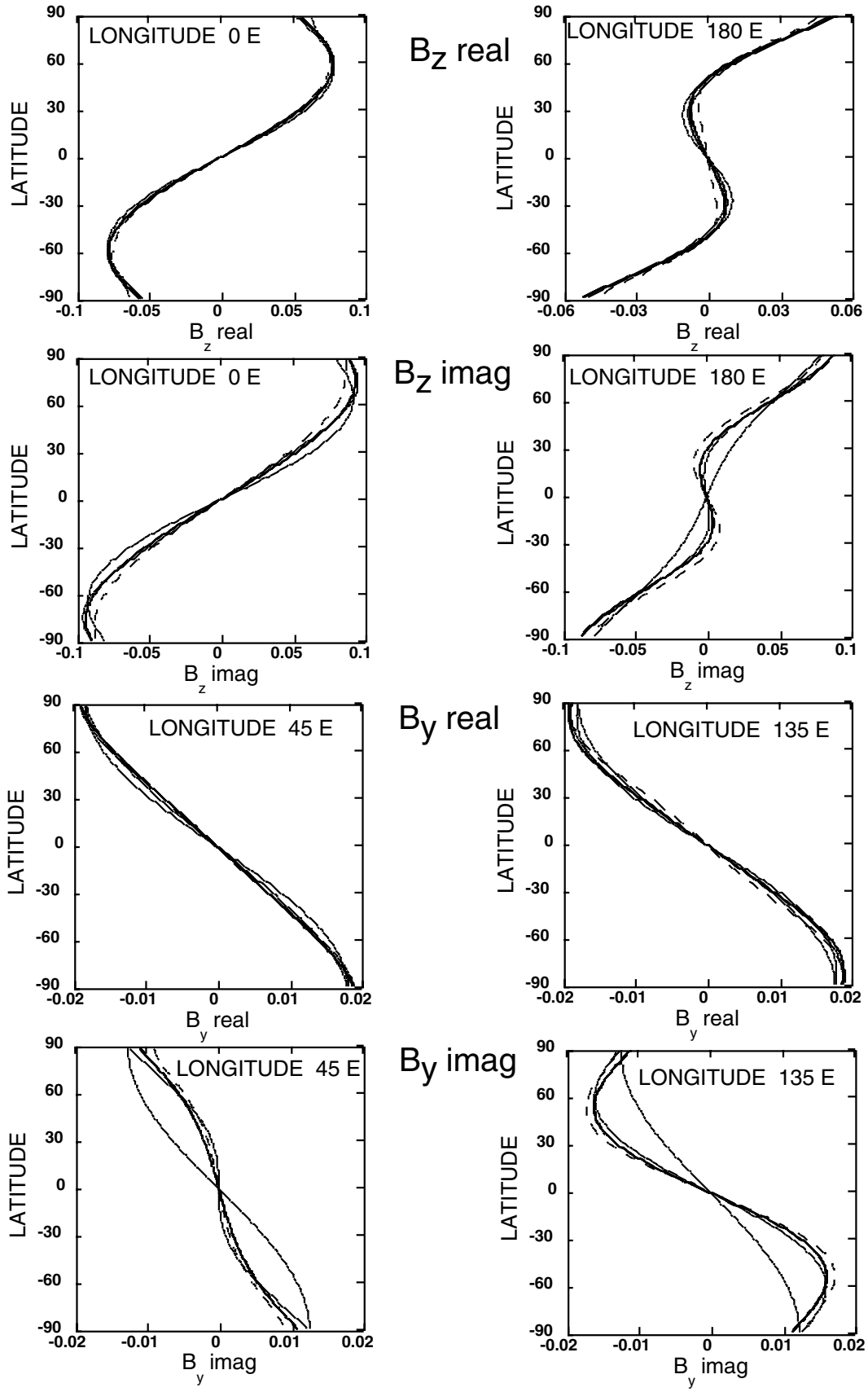


**Figure 9.** Comparison of the latitudinal variations of the response functions in frequency domain between TDM (thick solid curves) and FDM (thick dashed curves). Thin solid curves denote the fields composed from the Gauss coefficients up to harmonic degrees 2, 4, 6 and 8. Real and imaginary parts of $B_z$ at 0E and 180E, $B_y$ at 45E and 135E are shown.

real (in phase) and imaginary (out of phase) parts of the spatial distribution of the induced magnetic field ($B_z$ and $B_y$) in frequency domain were calculated by cosine and sine transforms, respectively, and compared with those calculated based on the staggered-grid finite difference method (FDM solution, Uyeshima & Schultz 2000).

In Fig. 8, real and imaginary parts of the surface response functions of $B_z$ (downward) and $B_y$ (eastward) for the period of 12 hr are compared. In the staggered-grid finite difference calculation, the radial structure of the model is the same as shown in Fig. 1 (Model400), and the horizontal variations of the electric conductivity were given at the mesh points with a grid spacing of 10 degrees. It is worth noting that the spatial distribution of $B_z$ will show no longitudinal dependence, and $B_y$ is zero all over the surface without the surface heterogeneous layer. The features of $B_z$ observed in the ocean hemisphere and $B_y$ are all generated by the existence of the surface layer. Fig. 8 indicates that the surface induced phases are equally observed in the results of the both approaches.

In order to compare the results of the both approaches in more detail, latitudinal variations of $B_y$ and $B_z$ at some longitudes are plotted in Fig. 9. The response functions reasonably agree and the root mean square value of the difference normalized by the amplitude of the variation along each meridian are 1.3 per cent ($B_z$ real 0 E), 2.6 per cent ($B_z$ real, 180 E), 2.9 per cent ($B_z$ imag, 0 E), 3.5 per cent ($B_z$ imag 0 E), 0.3 per cent ($B_y$ real, 45 E), 2.8 per cent ($B_y$ real, 135 E), 3.4 per cent ($B_y$ imag, 45 E), and 3.0 per cent ($B_y$ imag, 135 E), respectively. The relatively large deviations are observed near (180 E, 0 N) and the poles. In Fig. 9, the geomagnetic field constructed from the Gauss coefficients up to degrees 2, 3, 4, 5, 6, 8 obtained from the present calculation are also shown. The induced fields constructed by using the coefficients higher than degree 6 are identical with each other. Hence, we conclude that the difference between the TDM and FDM approach is not due to the truncation of spherical harmonics. The comparison in Fig. 9 indicates that the shorter wavelength components are more dominant in the FDM solution compared to the present time domain analysis. In the present approach (TDM), the spatial variation of the electrical conductivity is continuous, whereas the variation is discontinuous in the FDM calculation. Hence, the cause of the short-scale difference of the two methods can be attributed to the discrete nature of the conductivity structure in the FDM method. On the other hand, long wavelength deviation is probably due to the finite length of the Fourier transform of the TDM solutions.

It is to be noted that the appreciable amount of the higher degree components originally excited in the surface layer exist even at the period of 12 hr in the conductive ocean hemisphere. The significant deviation of the response functions from the radially symmetric Earth shown in Figs 7 and 8 indicates that the surface layer should be taken into consideration to investigate the heterogeneous structure in the deeper part of the mantle.

## 4 CONCLUSIONS

We have developed a time domain method to compute the electromagnetic induction response of an arbitrary 3-D conducting sphere by external sources. The method permits conductivity heterogeneities inside the Earth to calculate the transient response of the Earth to the external geomagnetic disturbances. The present approach provides the time-domain response function for each spherical harmonic component separately, which is convenient to solve the inverse problem for the global structure of the Earth, because the output from the spherical harmonic analysis separating the internal and the external components of the geomagnetic field can be directly fed to the investigation of the conductivity structure. The spherical analysis is also helpful to remove the short wavelength disturbances due to the surface distribution of oceans and continents. Frequency domain response functions were calculated from the present time domain solutions and compared with the results of the staggered grid finite difference methods by Uyeshima & Schultz (2000). The agreement is reasonably good, suggesting that the present method is also efficient for calculating the frequency domain response functions.

## ACKNOWLEDGMENTS

We are indebted to M. Uyeshima for calculating the response functions of the present three-layer mantle model with the staggered grid finite difference method.

## REFERENCES

Abramowitz, M. & Stegun, I.A., 1965. *Handbook of Mathematical Functions,* Dover, New York.

Achache, J., Le Mouel, J.L. & Courtillot, V., 1981. Long period geomagnetic variations and mantle conductivity: an inversion using Bailey method, *Geophys. J. R. astr. Soc.,* **65,** 579–601.

Banks, R.J., 1969. Geomagnetic variations and the electrical conductivity of the upper mantle, *Geophys. J. R. astr. Soc.,* **266,** 123–192.

Chapman, S. & Bartels, J., 1940. Electromagnetic induction within the Earth, in *'Geomagnetism,'* Vol. 2, pp. 711–749, Clarendon Press, Oxford.

Constable, S., 1993. Constraints on mantle electrical conductivity from field and laboratory measurements, *J. Geomag. Geoelectr.,* **45,** 707–728.

Egbert, G.D. & Booker, J.R., 1992. Very long period magnetotellurics at Tucson observatory: implications for mantle conductivity, *J. geophys. Res.,* **97,** 15 099–15 112.

Everett, M.E. & Schultz, A., 1996. Geomagnetic induction in a heterogeneous sphere: azimuthally symmetric test computations and the response of an undulating 660-km discontinuity, *J. geophys. Res.,* **101,** 2765–2783.

Fainberg, E.B., Kuvshinov, A.V. & Singer, B.Sh., 1990a. Electromagnetic induction in a spherical earth with non-uniform oceans and continents in electric contact with the underlying medium—I Theory, method and example, *Geophys. J. Int.,* **102,** 283–286.

Fainberg, E.B., Kuvshinov, A.V. & Singer, B.Sh., 1990b. Electromagnetic induction in a spherical Earth with non-uniform oceans and continents in electric contact with the underlying medium-II. Bimodal global geomagnetic sounding of the lithosphere, *Geophys. J. Int.,* **102,** 283–286.

James, R.W., 1973. The Adams and Elsasser dynamo integrals, *Proc. R. Soc. Lond.,* **A331,** 469–478.

Kuvshinov, A.V., Pankratov, O.V. & Singer, B.Sh., 1990. The effect of the oceans and sedimentary cover on global magnetovariational field distribution, *Pure appl. Geophys.,* **134,** 533–540.

Kuvshinov, A.V., Avdeev, D.B. & Pankratov, O.V., 1999. Global induction by Sq and Dst sources in the presence of oceans: bimodal solutions for non-uniform spherical surface shells above radially symmetric earth models in comparison to observations, *Geophys. J. Int.,* **137,** 630–650.

Lahiri, B.N. & Price, A.T., 1939. Electromagnetic induction in non-uniform conductors, and the determination of the conductivity of the Earth from terrestrial magnetic variations, *Phil. Trans. R. Soc. Lond.,* A., **A237,** 509–540.

Martinec, Z., 1999. Spectral-finite element approach to three-dimensional electromagnetic induction in a spherical Earth, *Geophys. J. Int.,* **136,** 229–250.

Olsen, N., 1999. Long-period (30 days-1year) electromagnetic sounding and the electrical conductivity of the lower mantle beneath Europe, *Geophys. J. Int.,* **138,** 179–187.

Parker, R.L., 1970. The inverse problem of electrical conductivity in the mantle, *Geophys. J. R. astr. Soc.,* **22,** 121–138.

Petersons, H.F. & Constable, S., 1996. Global mapping of the electrically conductive lower mantle, *Geophys. Res. Lett.,* **23,** 1461–1464.

Schultz, A., 1990. On the vertical gradient and lateral heterogeneity in midmantle electrical conductivity, *Phys. Earth planet. Int.,* **64,** 68–86.

Schultz, A., Kurtz, R.D., Chave, A.D. & Jones, A.G., 1993. Conductivity discontinuities in the upper mantle beneath a stable craton, *Geophys. Res. Lett.,* **20,** 2941–2944.

Schultz, A. & Pritchard, G. A three-dimensional inversion for large-scale structure in a spherical domain, in *Three-Dimensional Electromagnetics, Geophysical Development Series 7,* ed. Spies, B. & Oristiglaino.

Tarits, P., 1994. Electromagnetic studies of global geodynamic processes, *Surv. Geophys.,* **15,** 209–238.

Tarits, P. & Grammatica, N., 2000. Electromagnetic induction effects by the solar quiet magnetic field at satellite altitude, *Geophys. Res. Lett.,* **27,** 4009–4012.

Uyeshima, M. & Schultz, A., 2000. Geoelectromagnetic induction in a heterogeneous sphere: a new three-dimensional forward solver using a conservative staggered-grid finite difference method, *Geophys. J. Int.,* **140,** 636–650.

Zhang, T.S. & Schultz, A., 1992. A three-dimensional perturbation solution for the EM induction problem in a spherical earth—the forward problem, *Geophys. J. Int.,* **111,** 319–334.

## APPENDIX A: DERIVATION OF $P_n^k P_l^m = \sum_{s=0}^{\left[\frac{n+l-(k+m)}{2}\right]} \left(Q_{l,m}^{n,k}\right)_s P_{n+l-2s}^{k+m}$

The associated Legendre functions with Schmidt normalization satisfy the following recursive relations:

$$\begin{aligned}\cos\theta P_n^m &= \frac{u_{n+1}^m}{2n+1} P_{n+1}^m + \frac{u_n^m}{2n+1} P_{n-1}^m \\ \sin\theta P_n^m &= \frac{v_{n+1}^{m+1}}{2n+1} P_{n+1}^{m+1} + \frac{v_{n+1}^{-(m+1)}}{2n+1} P_{n-1}^{m-1},\end{aligned} \tag{A1}$$

where the coefficients $u_n^m$ and $v_n^m$ are given by

$$\begin{aligned}u_n^m &= [(n-m)(n+m)]^{\frac{1}{2}} \\ v_n^m &= \left[\frac{\varepsilon_{m-1}}{\varepsilon_m}(n+m)(n+m-1)\right]^{\frac{1}{2}}.\end{aligned} \tag{A2}$$

By using the above relation recursively, $\cos^k\theta P_n^m$ and $\sin^k\theta P_n^m$ can be expressed as

$$\begin{aligned}\cos^k\theta P_n^m &= \sum_{r=0}^{\left[\frac{n-m+k}{2}\right]\le k} C_r^{(k)} P_{n+k-2r}^m, \\ \sin^k\theta P_n^m &= \sum_{r=0}^{\left[\frac{n-m+k}{2}\right]\le k} S_r^{(k)} P_{n+k-2r}^{m+k},\end{aligned} \tag{A3}$$

where

$$\begin{aligned}C_r^{(k)} &= \frac{u_{n+k+1-2r}^m}{2(n+k+1-2r)+1} C_{r-1}^{(k-1)} + \frac{u_{n+k-2r}^m}{2(n+k-1-2r)+1} C_r^{(k-1)}, \\ S_r^{(k)} &= -\frac{v_{n+k+2-2r}^{-(m+k)}}{2(n+k+1-2r)+1} S_{r-1}^{(k-1)} + \frac{v_{n+k-2r}^{m+k}}{2(n+k-1-2r)+1} S_r^{(k-1)}.\end{aligned} \tag{A4}$$

The associated Legendre functions are defined as

$$\begin{aligned}P_N^M &= \sum_{r=0}^{\left[\frac{N-M}{2}\right]} q_r^{n.m} \sin^m\theta \cos^{N-M-2r}\theta, \\ q_r^{n.m} &= \left[\varepsilon_m \frac{(n-m)!}{(n+m)!}\right]^{\frac{1}{2}} \frac{(-1)^r}{r!2^r} \frac{(2n-2r-1)!!}{(n-m-2r)!},\end{aligned} \tag{A5}$$

where $[\frac{N-M}{2}]$ denotes the maximum integer which does not exceed $\frac{N-M}{2}$; $\varepsilon_m = 2$ for $m \neq 0$ and $\varepsilon_0 = 1$. Hence, the product of two Legendre functions can be calculated from the above relations of (A3) and (A5) as

$$P_N^M P_n^m = \sum_{r=0}^{\left[\frac{N-M}{2}\right]} q_r^{N.M} \sin^M\theta \cos^{N-M-2r}\theta P_n^m = \sum_{r=0}^{\left[\frac{N-M}{2}\right]} q_r^{N.M} \left\{ \sum_{t=0}^{\left[\frac{n+N-2r-(m+M)}{2}\right]} \left[S^{(M)} C^{(N-M-2r)}\right]_t^{n,n} P_{n+N-2r-2t}^{m+M} \right\}. \tag{A6}$$

By changing the order of summation, eq. (A6) becomes as

$$P_N^M P_n^m = \sum_{s=0}^{\left[\frac{N+n-(M+m)}{2}\right]} \left(Q_{n,m}^{N,M}\right)_s P_{N+n-2s}^{M+m}, \tag{A7}$$

where $(Q_{n,m}^{N,M})_s$ can be calculated from the relation:

$$\left(Q_{n,m}^{N,M}\right)_s = \sum_{r=0}^{\left[\frac{N-M}{2}\right]\le \begin{cases} s \\ N-s \end{cases}} q_r^{N,M} \left[S^{(M)} C^{(N-M-2r)}\right]_{s-r}^{n,m}. \tag{A8}$$

## APPENDIX B: DERIVATION OF $P_n^k P_l^m = \sum_{s=0}^{\left[\frac{n+l-|k-m|}{2}\right]} \left(R_{l,m}^{n,k}\right)_s P_{n+l-2s}^{|k-m|}$

From the definition of the associated Legendre functions shown in eq. (A5), $P_n^{m+M}$ can be expressed as

$$P_n^{m+M} = \left[\varepsilon_{m+M} \frac{(n-m-M)!}{(n+m+M)!}\right]^{\frac{1}{2}} \sum_{r=0}^{\left[\frac{n-(m+M)}{2}\right]} \frac{(-1)^r}{r!2^r} \frac{(2n-2r-1)!!}{(n-m-M-2r)!} \sin^{m+M}\theta \cos^{n-m-M-2r}\theta. \tag{B1}$$

By using the following relation,

$$\sin^{2M}\theta = (1-\cos^2\theta)^M, \tag{B2}$$

(B1) can be expressed as

$$P_n^{m+M} = \sum_{t=0}^{\left[\frac{n-|m-M|}{2}\right]} y_t^{n,m+M} \sin^{|m-M|}\theta \cos^{n-|m-M|-2t}\theta,$$

$$y_t^{n,m+M} = \left[\varepsilon_{m+M} \frac{(n-m-M)!}{(n+m+M)!}\right]^{\frac{1}{2}} (-1)^{M+t} \sum_{r=0}^{t} \frac{M!}{(M-t+r)!(t-r)!} \frac{(-1)^r}{r!2^r} \frac{(2n-2r-1)!!}{(n-m-M-2r)!}. \tag{B3}$$

Since $P_n^{|m-M|}$ is defined as

$$P_n^{|m-M|} = \sum_{t=0}^{\left[\frac{n-|m-M|}{2}\right]} z_t^{n,|m-M|} \sin^{|m-M|}\theta \cos^{n-m-M-2t}\theta,$$

$$z_t^{n,|m-M|} = \left[\varepsilon_{|m-M|} \frac{(n-|m-M|)!}{(n+|m-M|)!}\right]^{1/2} \frac{(-1)^t}{t!2^t} \frac{(2n-2t-1)!!}{(n-m-M-2t)!}, \tag{B4}$$

$P_n^{m+M}$ can be expressed with the linear combinations of $P_{n-2s}^{|m-M|}$ as

$$P_n^{m+M} = \sum_{s=0}^{\left[\frac{n-|m-M|}{2}\right]} w_s^{n,|m-M|} P_{n-2s}^{|m-M|},$$

$$w_s^{n,|m-M|} = \frac{1}{z_0^{n-2s,|m-M|}} \left\{ y_s^{n,|m-M|} - \sum_{t=0}^{s-1} w_t z_{s-t}^{n-2t,|m-M|} \right\}. \tag{B5}$$

Then, substituting the relation to eq. (A7), we get

$$P_n^k P_l^m = \sum_{r=0}^{\left[\frac{n+l-(m+k)}{2}\right]} \left(Q_{l,m}^{n,k}\right)_r \sum_{t=0}^{\left[\frac{n+l-2r-|m-k|}{2}\right]} w_t^{n+l-2r,|m-k|} P_{n+l-2r-2t}^{|m-k|} = \sum_{s=0}^{\left[\frac{n+l-|m-k|}{2}\right]} \left\{ \sum_{r=0}^{s} \left(Q_{l,m}^{n,k}\right)_r w_{s-r}^{n+l-2r,|m-k|} \right\} P_{n+l-2s}^{|m-k|} = \sum_{s=0}^{\left[\frac{n+l-|m-k|}{2}\right]} \left(R_{l,m}^{n,k}\right)_s P_{n+l-2s}^{|m-k|},$$

$$(s = r+t) \tag{B6}$$

and $(R_{l,m}^{n,k})_s$ can be expressed by the linear combination of $(Q_{l,m}^{n,k})_r$ as

$$\left(R_{l,m}^{n,k}\right)_s = \sum_{r=0}^{s} \left(Q_{l,m}^{n,k}\right)_r w_{s-r}^{n+l-2r,|m-k|}, \tag{B7}$$

where the coefficients $w_{s-r}^{n+l-2r,|m-k|}$ is defined in (B5).